Journal of Materials Chemistry C

ROYAL SOCIETY OF CHEMISTRY

PAPER

View Article Online
View Journal | View Issue

Cite this: J. Mater. Chem. C, 2024, 12, 16422

A novel near-infrared phosphor $Li_{1.6}Mg_{1.6}Sn_{2.8}O_8:Cr^{3+}$ for near-infrared spectral analysis†

Xiaowei Zhang,[ab] Dashuai Sun,[b] Pengcheng Luo,[b] Luhui Zhou,[b] Xinyu Ye *[a] and Hongpeng You *[b]

Received 13th July 2024,
Accepted 2nd September 2024

DOI: 10.1039/d4tc02979h

rsc.li/materials-c

Near infrared (NIR) phosphors have a wide emission range, high quantum yield and good absorption efficiency, which can meet the detection needs of different wavelengths in the NIR spectrum, exhibiting great developmental potential. In this study, a novel near-infrared phosphor $Li_{1.6}Mg_{1.6}Sn_{2.8}O_8:Cr^{3+}$ (referred to as LMSO:Cr^{3+}) has been developed, with a near-infrared emission wide-band from 600 to 1200 nm, a peak at 860 nm, and a full width at half maximum of 187 nm. It possesses an internal quantum efficiency of 51.6% and a high absorption efficiency of 59%, leading to an external quantum efficiency of 30.7%. A NIR pc-LED device prepared using this material can achieve a high NIR output power of 25.20 mW at a driving current of 100 mA and a photoconversion efficiency of 14.71% at a driving current of 10 mA, exhibiting excellent performance in near-infrared spectroscopic detection, penetration of biological tissues, and night vision imaging.

1 Introduction

A near infrared (NIR) spectroscopy analyzer is an instrument for the quantitative analysis of samples using specific absorption spectra of molecular compounds. When a sample is illuminated with NIR light (usually 650 to 1050 nm), part of the NIR light is reflected and another part is absorbed. The reflection–absorption ratio varies from sample to sample, so that the content of relevant components in the sample can be determined. The wider the wavelength coverage of the NIR light source, the more objects can be analyzed. The integration of NIR analyzers into mobile phones or wearable devices to broaden the usage scenarios of NIR detection is an emerging market demand, which requires small size, broadband NIR light sources. The traditional tungsten halogen lamp or supercontinuum laser cannot meet the market demand due to the shortcomings of large volume and low efficiency. In this context, a NIR phosphor conversion light emitting diode (pc-LED), which is prepared by coating one or more NIR phosphors on a blue LED chip, has attracted wide attention. Therefore, high-efficiency broadband NIR phosphors, which convert blue light from LED chips to NIR light, are critical to the luminescent performance of pc-LED light sources.[1,2]

Recently, numerous NIR phosphors doped with various ions have been developed. Some rare-earth ions, such as Nd^{3+}, Ho^{3+}, Er^{3+}, Tm^{3+} and Yb^{3+}, show NIR emissions due to their abundant energy levels. However, the weak absorption capabilities yield low luminescence efficiency owing to the predominance of parity-forbidden f–f transitions in these rare earth ions. Transition metal ion activators such as Fe^{3+}, Ni^{2+}, and $Cr^{3+}/^{4+}$ present an alternative avenue to fulfill near-infrared light requisites.[3–8] Among them, the Cr^{3+} ion has a $3d^3$ electron configuration, and its shell does not shield three valence electrons. In a weak crystal field, its broadband emission is attributed to the spin-allowed $^4T_2 \rightarrow {}^4A_2$ transition that predominates with an absorption band covering almost the entire UV-visible range, making it an ideal center for near-infrared luminescence.[9,10] For example, the broadband near-infrared phosphor $Mg_2LaTaO_6:Cr^{3+}$ exhibits a broadband emission with a peak at 815 nm and a full width at half maximum (FWHM) of 203 nm, coupled with an internal quantum efficiency (IQE) of 85.6%, and $Mg_7Ga_2GeO_{12}:Cr^{3+}$ emits ultra-broadband near-infrared light centered at 808 nm (FWHM of 226 nm) with an excellent quantum yield (QY) of 93.4%.[11,12] Despite their high quantum efficiency and thermal stability, the optimal emission peaks of these phosphors are all below 850 nm. $La_2MgZrO_6:Cr^{3+}$ showed far-red emission in the range of 700–1100 nm, with FWHM of 210 nm, and IQE and EQE of 56% and 18%, respectively.[13] $LiScSnO_4:Cr^{3+}$ emits from 700 to 1400 nm (λ_{max} = 900 nm) with a FWHM of 227 nm. The IQE is only 18.8%.[14]

[a] College of Rare Earths, Jiangxi University of Science and Technology, Ganzhou, Jiangxi 341000, P. R. China. E-mail: xinyye@yahoo.com
[b] Key Laboratory of Rare Earths, Chinese Academy of Sciences, Ganjiang Innovation Academy, Chinese Academy of Sciences, Ganzhou 341000, P. R. China. E-mail: hpyou@ciac.ac.cn

† Electronic supplementary information (ESI) available. See DOI: https://doi.org/10.1039/d4tc02979h

$NaZn(PO_3)_3:Cr^{3+}$ emission was in the range of 700–1300 nm (λ_{max} = 900 nm), and the FWHM is 218 nm, while the luminescence total intensity at 378 K is only 44.1% of its value at room temperature.[15] However, these long-wavelength emitting (emission peak > 850 nm) NIR phosphors, due to giant Stokes shift, either have low quantum efficiency values or inadequate thermal stability. As a result, it is essential to manufacture long-wavelength, ultra-broadband Cr^{3+}-activated phosphors with high QE to meet the requirements of broadband NIR pc-LEDs for NIR spectroscopy analysis. In this study, we report a new broadband NIR phosphor $Li_{1.6}Mg_{1.6}Sn_{2.8}O_8:Cr^{3+}$ (For simplicity, labeled as LMSO:Cr^{3+}). Furthermore, by adjusting the Cr^{3+} doping concentration, the emission peak can be effectively shifted towards longer wavelength, enabling the sample to achieve long-wavelength emission while maintaining relatively high quantum efficiency and great thermal stability. Among them, the LMSO:0.06Cr^{3+} sample exhibits a wide NIR emission band peaking at 860 nm with a FWHM of 187 nm. The IQE and AE of the LMSO:0.06Cr^{3+} sample are 53.77% and 59%, respectively, resulting in an EQE of 31.72% under 435 nm excitation. Furthermore, we fabricated NIR pc-LEDs with a NIR output power of 25.20 mW@100 mA and an optimal photoelectric conversion efficiency of 14.71%@10 mA, demonstrating its application in the field of biological imaging and non-destructive detection.

2 Experimental section

2.1 Materials and preparation

A series of NIR luminescence phosphors $Li_{1.6}Mg_{1.6-0.5x}Sn_{2.8-0.5x}O_8:xCr^{3+}$ (LMSO:xCr^{3+}) (x = 0.02 0.04, 0.06, 0.08, 0.10, 0.12, 0.15) were synthesized by high temperature solid-state reaction. The raw materials including MgO (99.99%), SnO_2 (99.8%), and Cr_2O_3 (99.99%) were weighed in stoichiometric ratio and a 5% excess of Li_2CO_3 (99.99%) was used for evaporation losses during sintering. Then, the raw materials were thoroughly mixed with appropriate ethanol in an agate mortar for 20 minutes. The mixtures were then transferred to alumina crucibles and sintered at 800 °C for 4 h in the air, then reground into fine powders and sintered at 1250 °C for 4 h under an air atmosphere. Eventually, the samples were cooled down to room temperature inside the furnace and then finely ground for characterization purposes.

2.2 NIR pc-LED device fabrication

Near-infrared (NIR) pc-LEDs were fabricated by integrating the synthesized LMSO:0.06Cr^{3+} phosphor with a blue InGaN chip (450 nm). In a standard fabrication procedure, the LMSO:0.06Cr^{3+} phosphor was uniformly blended with silicone resins A and B (A : B = 1 : 1) using an onyx mortar, and the resulting mixture was applied onto a blue InGaN chip (450 nm).

2.3 Characterization

The X-ray diffraction (XRD) spectra were obtained using a Bruker AXS D8 X-ray diffractometer, employing a Cu Kα radiation source (λ = 0.15406 nm). The test was conducted over a scan range of 10° to 80° with a step size of 0.02° s^{-1}, under a voltage of 40 kV and a current of 40 mA. XRD refinement analysis was conducted using the general structure analysis system (GSAS) software, created by A. C. Larson and R. B. Von Dreele. A field-emission scanning electron microscope (SEM, S 4800, Hitachi, Japan) was employed to analyze the morphology and conduct energy-dispersive X-ray spectroscopy (EDS). Diffuse reflection spectra (DRS) were obtained using a Shimadzu UV-3600 Plus spectrophotometer, manufactured by Shimadzu in Japan. The photoluminescence (PL) and photoluminescence (PLE) spectra at room temperature (RT) were measured using an FLS 1000 fluorescence spectrophotometer (Edinburgh Instruments, UK) with the lamp as the excitation source and equipped with a near infrared PMT detector. PL attenuation curves were obtained by the same FLS 1000 fluorescence spectrophotometer with a microsecond flash (μF900) as the excitation light source. The photoelectric properties of the pc-LEDs were analyzed using an integrating sphere spectroradiometer (HASS-2000, 350–1650 nm, Everfine).

3 Results and discussion

3.1 Crystal structure and morphology

Fig. 1a illustrates the XRD patterns of the LMSO:xCr^{3+} (x = 0.02–0.15) samples. The diffraction peaks observed in the samples closely correspond to the standard pattern ICSD.100590 ($Li_{1.6}Mg_{1.6}Sn_{2.8}O_8$), indicating the formation of a pure phase. A magnified view of the XRD pattern in the range of 34–36° shows that the positions of the diffraction peaks shift to larger angles as the Cr^{3+}-concentration increases. This phenomenon can be elucidated by Bragg's equation, $2d\sin\theta = n\lambda$. Since the ionic radius of Cr^{3+} in the octahedron is smaller than those of Mg^{2+} and Sn^{4+}, the lattice volume shrinks with the increase in Cr^{3+} concentration. As a result, the interplanar spacing decreases, leading to an increase in θ. Considering the valence states and ionic radii among Li^+ (0.76 Å, CN = 6), Mg^{2+} (0.72 Å, CN = 6), and Sn^{4+} (0.69 Å, CN = 6), it is expected that the smaller Cr^{3+} ions (radius = 0.62 Å, CN = 6) will randomly occupy the Mg^{2+} and Sn^{4+} sites in the lattice. A strategy has been implemented to balance the charge imbalance resulting from the random occupancy of Cr^{3+} ions, where every two Cr^{3+} ions substitute for one Mg^{2+} ion and one Sn^{4+} ion, resulting in the formation of the composition $Li_{1.6}Mg_{1.6-0.5x}Sn_{2.8-0.5x}O_8:xCr^{3+}$.

To further investigate the crystal structure of the synthesized samples, comprehensive Rietveld refinements were conducted for both LMSO and LMSO:0.06Cr^{3+} specimens using GSAS software. Initial parameters were derived from the standard card ICSD.100590 ($Li_{1.6}Mg_{1.6}Sn_{2.8}O_8$), as depicted in Fig. S1 (ESI†) and Fig. 1b. The detailed parameters of LMSO and LMSO:Cr^{3+} are R_p = 8.27%, R_{wp} = 9.89% and R_p = 7.04%, R_{wp} = 8.33%, respectively. The weighted and profile R-factors are below 10%, which validates the reliability of the Rietveld refinements. The crystal lattice parameters of $Li_{1.6}Mg_{1.6-0.5x}Sn_{2.8-0.5x}O_8:xCr^{3+}$ (x = 0 and 0.06) are listed in Table S1 (ESI†). Additionally, the atom positions, fraction factors, and thermal vibration parameters of $Li_{1.6}Mg_{1.6-0.5x}Sn_{2.8-0.5x}O_8:xCr^{3+}$

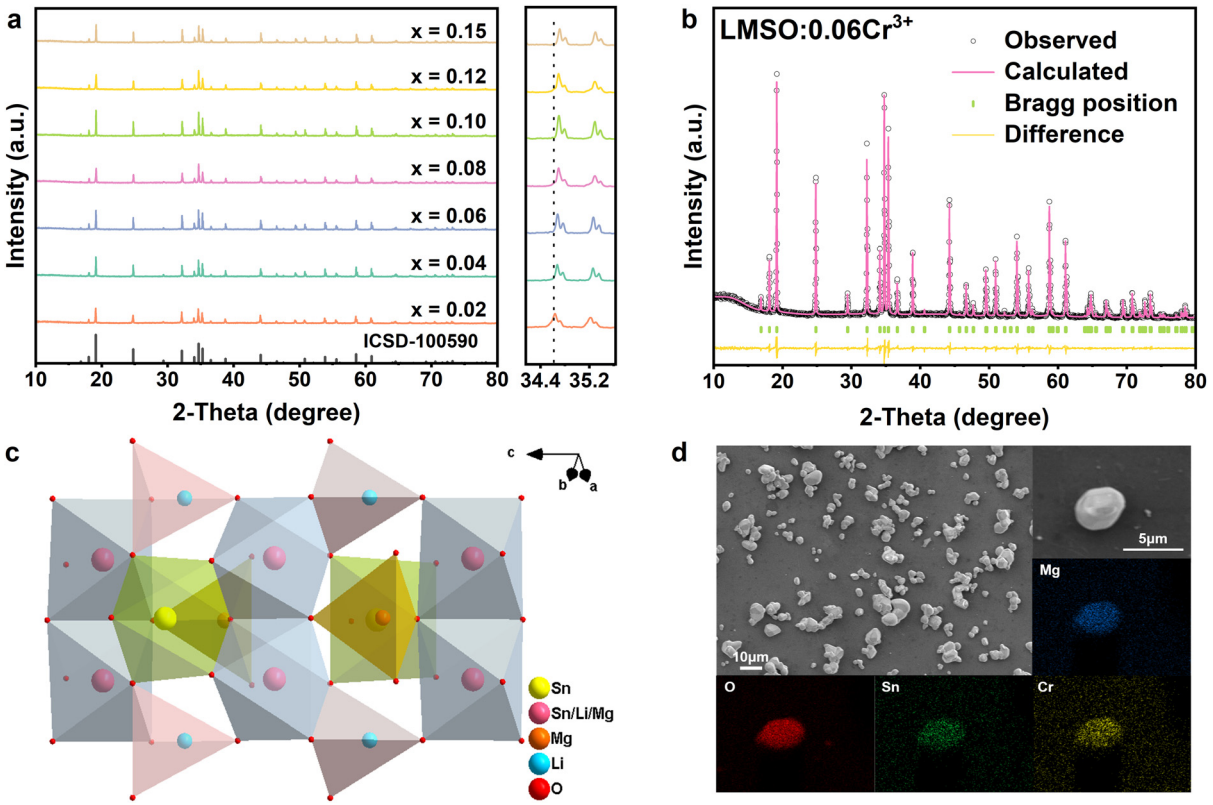

Fig. 1 (a) XRD patterns of LMSO:xCr^{3+} samples and magnified XRD patterns; (b) Rietveld refinement of LMSO:0.06Cr^{3+}; (c) crystal structure of LMSO; (d) LMSO:0.06Cr^{3+} morphology and elemental mapping.

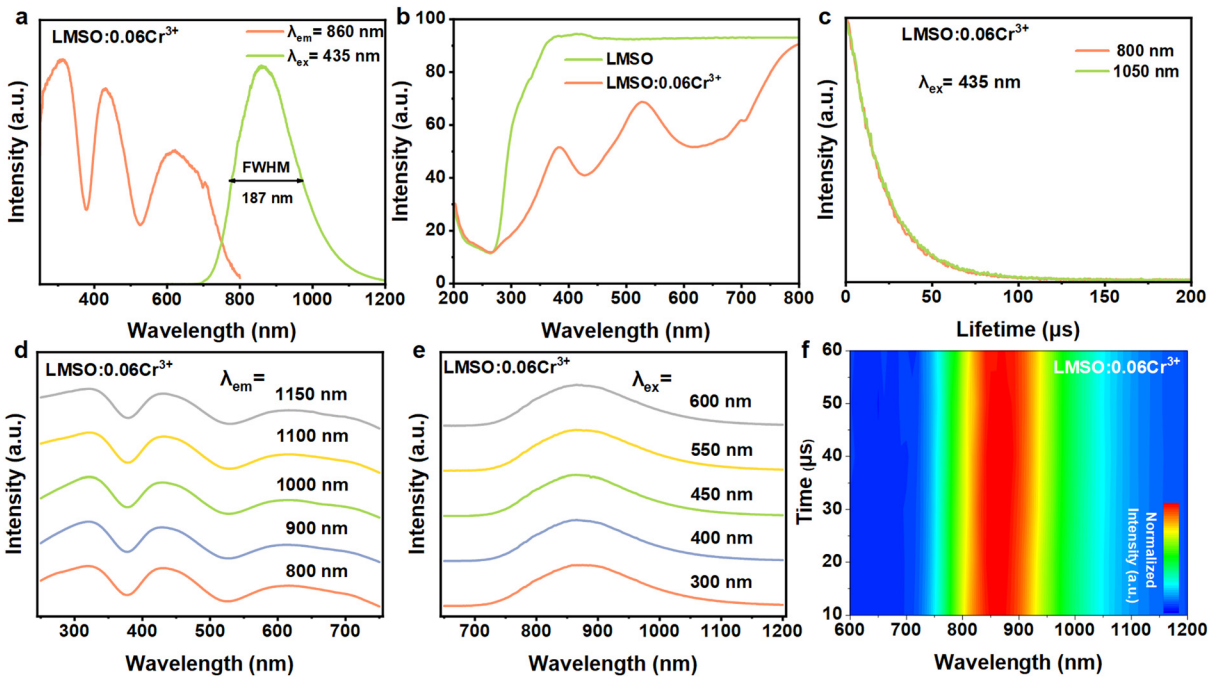

Fig. 2 (a) PLE and PL spectra of the LSMO:0.06Cr^{3+}; (b) UV-visible DRS of LSMO and LSMO:0.06Cr^{3+}; (c) luminescent decay curves of LMSO:0.06Cr^{3+}(-λ_{em} = 800 and 1050 nm); (d) normalized excitation spectra of LMSO:0.06Cr^{3+} monitored at different locations; (e) normalized emission spectra of LMSO:0.06Cr^{3+} under different excitations; (f) TRES mapping images of LMSO:0.06Cr^{3+}.

(x = 0 and 0.06) are listed in Table S2 (ESI†). The crystal structure of LMSO is shown in Fig. 1c, LMSO has a hexagonal crystal system with the space group of *P*63*mc*. Along the *c*-axis direction, the LMSO crystal consists of continuously repeating ABAB… forming a three-dimensional layered structure, where the A layer is made up of edge-sharing [Sn2/Li2/Mg2O6] octahedra, and the B layer is made up of corner-sharing [Li1O4] tetrahedra, [Mg1O4] tetrahedra and [Sn1O6] octahedra.

The morphology and elemental distribution of the synthesized phosphor were observed using SEM and EDS (Fig. 1d). The phosphor mainly consists of irregular-shaped particles ranging from 5 to 10 μm in size. Cr, O, Mg, and Sn are evenly distributed throughout the phosphor particles. The XPS of LMSO:0.06Cr^{3+} in Fig. S2 (ESI†) also confirms the presence of Li, Mg, Sn, O, and Cr in the sample, consistent with the results of elemental mapping. The enlarged XPS spectra reveal two peaks at 576.4 and 580.9 eV, corresponding to the binding energies of the Cr^{3+} ions in the Cr2p3/2 and Cr2p1/2 orbitals, respectively (Fig. S3, ESI†). These results confirm the uniform incorporation of Cr^{3+} ions into the host lattice.

Fig. 2a displays the PLE and PL spectra of the LMSO:0.06Cr^{3+} sample. Upon 435 nm excitation, the sample exhibits a broad near-infrared emission with a peak at 860 nm and a FWHM of 187 nm. Monitoring the PLE spectrum at 860 nm reveals three excitation bands situated at 310, 435 and 630 nm. These three bands also appear correspondingly in the DR spectrum of the LMSO:0.06Cr^{3+} sample (Fig. 2b). The excitation bands observed at 435 and 630 nm correspond to the $^4A_2 \rightarrow {}^4T_1$ (4F) and $^4A_2 \rightarrow {}^4T_2$ (4F) transitions of the Cr^{3+} ions, respectively. The absorption band at 310 nm is assigned to absorption by the host lattice and the $^4A_2 \rightarrow {}^4T_1$ (4P) transition of the Cr^{3+} ions, which aligns with the host lattice absorption band located at 265 nm in the DR spectrum of undoped LMSO. The fluorescence decay curves of the LMSO:0.06Cr^{3+} monitored at 800 and 1050 nm are shown in Fig. 2c. The two lifetime curves coincide completely, with a calculated lifetime value of 24.40 and 25.13 μs, respectively. This result means that the luminescence originates from the same type of Cr^{3+}-center. To understand whether multisite coexistence exists, we first separate excitations by monitoring several different positions of the wavelengths on either side of the emission band to prevent overlap. As depicted in Fig. 2d, the excitation spectra measured were adjusted for normalization, revealing nearly identical excitation spectra across different monitored positions. Additionally, Fig. 2e illustrates that the normalized emission spectra of LMSO:0.06Cr^{3+} at various excitation wavelengths are identical. For further confirmation, we measured the time-resolved emission spectra (TERS) of LMSO:0.06Cr^{3+} under pulsed xenon lamp excitation at 435 nm (Fig. 2f). The photoluminescence intensity decreases in tandem with the decay time, with no significant change in spectral shape observed. All the above results indicate that there is only one kind of Cr^{3+}-center in LMSO:0.06Cr^{3+}.

As mentioned in the crystal structure section above, there are two different octahedra in the LMSO matrix. As shown in Fig. 1c and Fig. S5 (ESI†), the number of [Sn2/Li2/Mg2O6] octahedra is three times the number of [Sn1O6] octahedra,

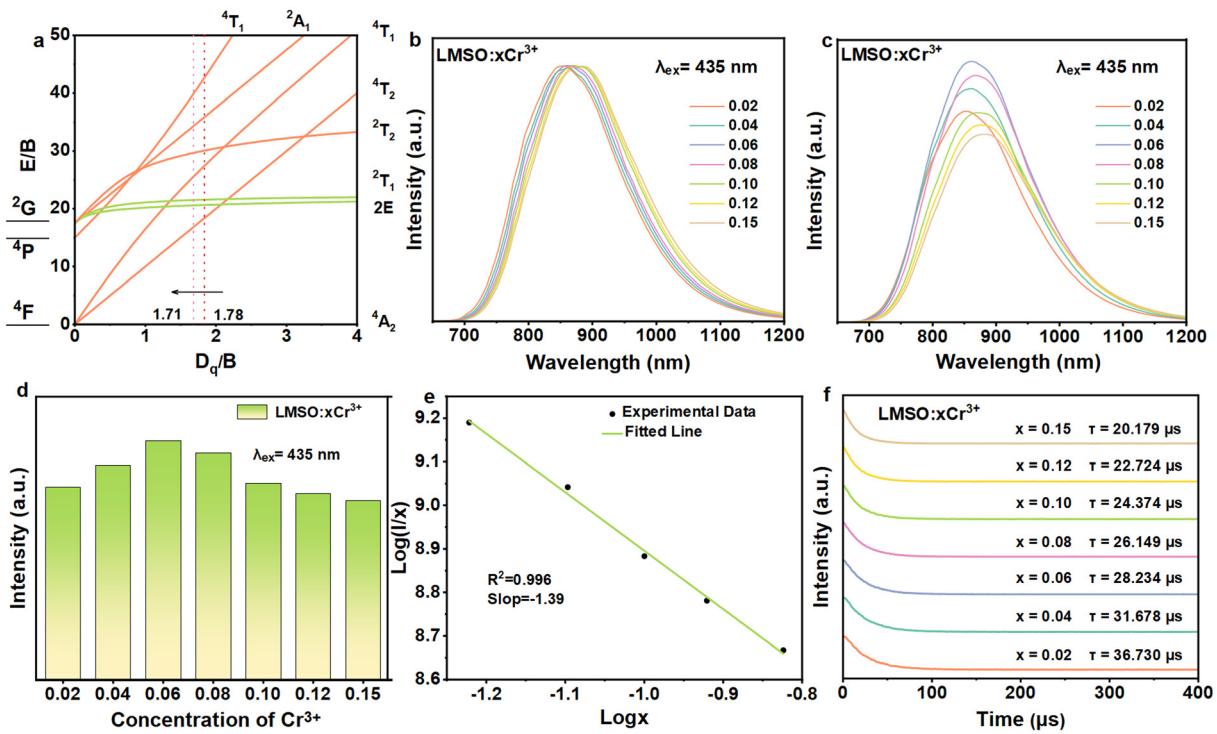

Fig. 3 (a) Tanabe–Sugano energy level diagram for Cr^{3+} ions ($3d^3$) in octahedral coordination; (b) normalized excitation spectra of LMSO:$x$$Cr^{3+}$ (x = 0.02 to 0.15); (c) normalized emission spectra of LMSO:$x$$Cr^{3+}$; (d) LMSO:$x$$Cr^{3+}$ emission intensity for various Cr^{3+} doping concentrations; (e) relationship of log(*I*/*x*) *versus* log(*x*) in LMSO:$x$$Cr^{3+}$ (x = 0.02 to 0.15); (f) PL decay time spectra.

and the average bond length of the [Sn2/Li2/Mg2O6] octahedra is smaller than that of the [Sn1O6] octahedra, and the average valence state of the central cations of the [Sn2/Li2/Mg2O6] octahedra is +3, the same as that of Cr^{3+} ions, while the charge state of the central cations of the [Sn1O6] octahedra is +4. Considering the above aspects, we believe that Cr^{3+} ions occupy the [Sn2/Li2/Mg2O6] octahedra site in the LMSO matrix.

The Cr^{3+} ion has d-electrons distributed in the outermost layer of the ion, making its energy level structure highly sensitive to the crystal field environment. Fig. 3a presents the Tanabe–Sugano energy level diagram. The D_q/B value of LMSO:0.06Cr^{3+} is approximately 1.77. This result shows that the Cr^{3+} ion is in a weak crystal field in the LMSO lattice. The calculations reveal that the crystal field strength weakens with an increase in Cr^{3+}-concentration, with D_q/B values of 1.78 and 1.71 for LMSO:0.02Cr^{3+} and LMSO:0.15Cr^{3+}, respectively (listed in Table S3, ESI†). As the Cr^{3+} doping concentration increases, a significant red shift can be observed in the normalized emission spectra shown in Fig. 3b, with the emission peak shifting from 850 to 882 nm. This phenomenon may be attributed to the higher Cr^{3+} doping concentration, which facilitates energy transfer between Cr^{3+} ions, leading to a red shift in the emission wavelength as the doping concentration increases. Additionally, when Cr^{3+} occupies [Li/Mg/Sn] sites, the average bond length slightly increases with higher doping concentration (from 2.1020 Å to 2.1023 Å), resulting in a decrease in D_q. The values of D_q and D_q/B calculated based on crystal field theory and spectral data also gradually decrease (listed in Table S3, ESI†), which further explains the observed red shift.[16–19]

To optimize the Cr^{3+}-doping concentration, the emission spectra of the LMSO:$x$$Cr^{3+}$ (x = 0.02 to 0.15) samples were measured under 435 nm excitation, as depicted in Fig. 3c. The maximum emission intensity of the Cr^{3+} ions is at x = 0.06 (in Fig. 3d). As the Cr^{3+} concentration increases further, the emission intensity diminishes as a result of concentration quenching. For further analysis of the concentration quenching mechanism, the critical distance (R_c) is computed from:[20]

$$R_c = 2\left(\frac{3V}{4\pi xN}\right)^{\frac{1}{3}} \quad (1)$$

where c denotes the critical concentration of the Cr^{3+} ions (c = 0.06), N denotes the number of cations in a single crystal cell (N = 2.4), and V represents the volume of the unit cell (V = 314.35 Å). The computed R_c is 16.08 Å, significantly greater than 5 Å.[21] Thus, the multipolar interaction plays a role in the energy transfer (ET) mechanism that contributes to the quenching effect observed in the sample. To further elucidate the concentration quenching mechanism, the critical distance was calculated using the following equation:[22]

$$\log(I/x) = A - \frac{\theta}{3}\log x \quad (2)$$

where x denotes the doping concentration of the Cr^{3+} ions, beginning from the optimal level. I is the luminescence intensity corresponding to the concentration and A is a constant. To determine the value of θ, the linear relationship between log(I/x) and log(x) is presented in Fig. 3e. From the slope of the fitted line, one can calculate that θ is 4.17, which is close to 6. Therefore, the

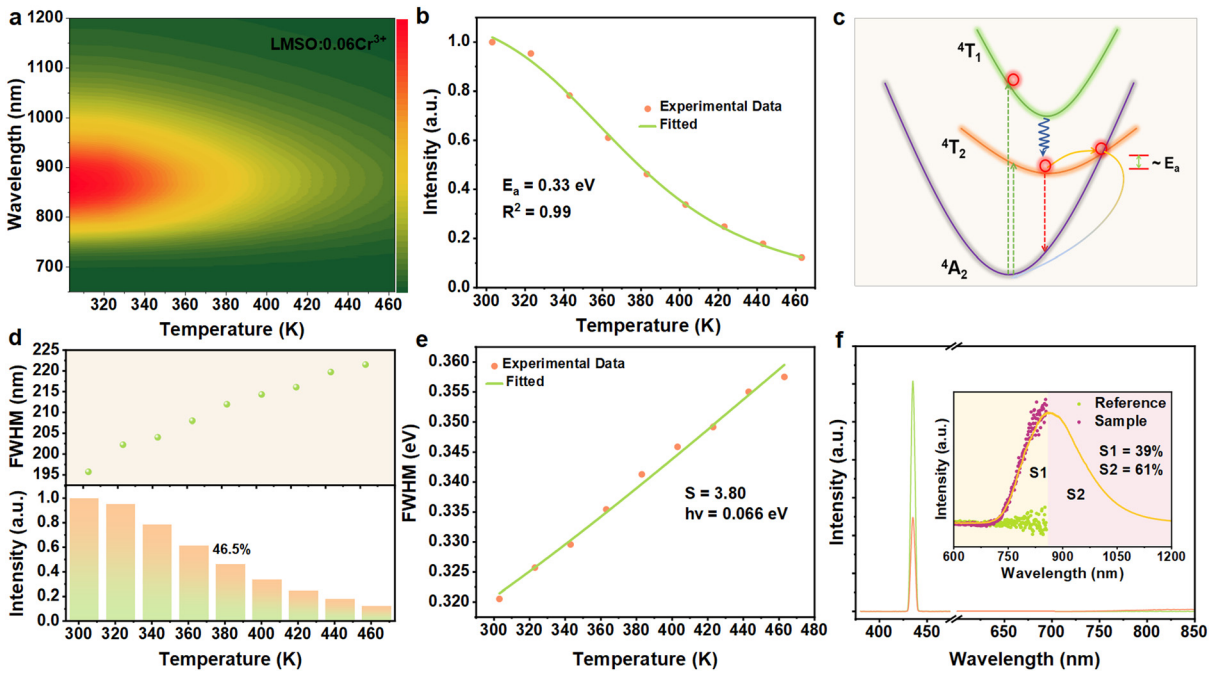

Fig. 4 (a) Temperature dependence of the LMSO:0.06Cr^{3+} emission spectra (303–463 K); (b) FWHM and emission intensity of LMSO:$x$$Cr^{3+}$ (x = 0.02–0.15); (c) Huang–Rhys factor (S) and the phonon energy ($\hbar\omega$) obtained through fitting the relationship between FWHM (eV) and T (K); (d) activation energy of LMSO:0.06Cr^{3+}; (e) configurational coordinate diagram of Cr^{3+} ions; (f) integrated intensity of LMSO:0.06Cr^{3+} for IQE measurements (Inset shows the integrated part S1 and the missing part S2).

energy transfer mechanism in the current system mainly involves both dipole–dipole interactions.[23] Fig. 3f shows the decay curves of LMSO:xCr^{3+} (x = 0.02–0.15) with detection at 860 nm and excitation at 435 nm. The obtained curves show a fluorescence decay pattern that follows a single exponential function:[24]

$$I = I_0 + A \cdot \exp\left(-\frac{t}{\tau}\right) \quad (3)$$

where I denotes the emission intensity and I_0 denotes initial emission intensity. A represents the fitting constant, and τ and t are the lifetime and the time, respectively. As the Cr^{3+}-concentration increases from 0.02 to 0.15 mol, the luminescence lifetime decreases from 31.97 to 19.36 μs. This can be due to the increased doping concentration, which enhances the possibility of the energy transfer from the Cr^{3+}-center to defects.

The thermal stability of phosphors in LED devices plays a crucial role in assessing their capability, as pc-LED devices can reach temperatures in the range of 80–160 °C during operation. When the emission peak wavelength exceeds 850 nm, near-infrared phosphors tend to exhibit severe thermal quenching, which has become a major constraint on the large-scale application of near-infrared pc-LEDs.[25] Fig. 4a depicts the emission spectrum of LMSO:0.06Cr^{3+} as a function of temperature, demonstrating its thermal stability. In combination with Fig. 4a and the LMSO:0.06Cr^{3+} temperature-dependent emission spectra (shown in Fig. S6, ESI†), the spectral distribution remains consistent, while the total emission intensity of the sample decreases with increasing temperature and remains at 46.5% of the initial emission intensity at 383 K. The thermal stability of LMSO:0.06Cr^{3+} is better than many previously reported near-infrared emitters with λ_{max} exceeding 800 nm, such as $Y_{0.57}La_{0.72}Sc_{2.71}(BO_3)_4$:Cr^{3+} ($\lambda_{max}$ = 850 nm, 41.07% at 373 K), Mg_2GeO_4:Cr^{3+} (λ_{max} = 940 nm, less than 10% at 410 K), and $LiInGe_2O_6$:Cr^{3+} (λ_{max} = 880 nm, about 20% at 410 K).[26–28] The thermal activation energy (E_a) is defined as the energy gap between the lowest excited state and the intersection point. E_a is a common measure for assessing the likelihood of non-radiative processes, determined through the Arrhenius equation.[29,30]

$$I(T) = \frac{I_0}{1 + c\exp\left(-\frac{E_a}{kT}\right)} \quad (4)$$

where $I(T)$ and I_0 represent the intensity at different temperatures and initial PL intensity, respectively; c denotes a constant; k denotes the Boltzmann constant (8.62×10^{-5} eV). According to eqn (4), the activation energy E_a was estimated to be 0.33 eV, as shown in Fig. 4b. The thermal quenching caused by non-radiative transitions is accounted for by the configuration coordinate illustration shown in Fig. 4c. With the temperature increases, electrons on the $^4T_2$ excitation state can easily undergo non-radiative relaxation to the $^4A_2$ ground state through the intersection point of the $^4T_2$ and $^4A_2$ parabolas, causing a reduction in emission intensity. As observed in Fig. 4d, the FWHM increases from 195 to 222 nm as the temperature rises from 303 K to 463 K. As the temperature increases, the vibrational amplitude and electron–phonon interactions enhance, resulting in a wider energy distribution and a broader emission band for the $^4T_2 \rightarrow {}^4A_2$ transition.[31] Next, we investigated the electron–phonon coupling (EPC) effect on thermal quenching, where the interaction between electrons and phonons is crucial for the thermal quenching process. The electron–phonon coupling effect is expressed by fitting the Huang–Rhys factor (S), which is obtained from the next equation:[17,32]

$$\mathrm{FWHM}\,(T) = \sqrt{8 \cdot \ln 2} \times \sqrt{S} \times \hbar\omega \times \sqrt{\coth\frac{\hbar\omega}{2kT}} \quad (5)$$

where the FWHM(T) represents the full width at half-maximum obtained from fitting each emission spectrum at temperature T (K), $\hbar\omega$ denotes the phonon energy, and k is Boltzmann's constant (8.617×10^{-5} eV K^{-1}). From Fig. 4e, $\hbar\omega$ and S are 0.066 eV and 3.80, respectively. Compared with other reported broadband near-infrared phosphors, the electron–phonon coupling in LMSO is relatively strong. In such a scenario, the phonon-assisted non-radiative relaxation process results in a significant loss of emission intensity at elevated temperatures. Fig. 4f shows the quantum efficiency of LMSO:0.06Cr^{3+} tested under optimal excitation. The IQE and EQE of the LMSO:0.06Cr^{3+} sample are approximately 20.97 and 12.37% respectively, with a measurement upper limit of 860 nm. When considering the S2 part, the IQE and EQE of the LMSO:0.06Cr^{3+} sample are calculated to be 53.77% and 31.72%, respectively. Considering its larger emission peak and broader FWHM in other near-infrared phosphors (Table 1), the IQE of LMSO:0.06Cr^{3+} is acceptable. Meanwhile, the absorption efficiency of LMSO:0.06Cr^{3+} is 59%, which is higher than that of most near-infrared phosphors. There are

Table 1 Photoelectric properties of the fabricated LED device based on some broadband NIR emission phosphors

Phosphor	λ_{max} (nm)	FWHM (nm)	IQE (%)	AE	Temperature (K)	NIR output power/photoelectric efficiency of pc-LED	Ref.
$Li_{1.6}Mg_{1.6}Mg_{2.8}O_8$:0.06Cr^{3+}	860	187	53.77	59	46.5%@383	25.20 mW/14.71%	This work
$Mg_2Al_4Si_5O_{18}$:0.02Cr^{3+}	856	200	—	—	45.2%@398	∼8 mW/—	33
La_2MgZrO_6:0.02Cr^{3+}	825	210	56	32	∼40%@383	—	13
$K_2Ga_2Sn_6O_{16}$:0.03Cr^{3+}	830	220	48	—	—	—	34
$Y_{0.57}La_{0.72}Sc_{2.71}(BO_3)_4$:0.025Cr^{3+}	850	172	41.1	—	42%@373	10.69 mW/—	28
$Sr_9Ga(PO_4)_7$:0.05Cr^{3+}	850	∼140	66.3	45	∼5%@423	6.67 mW/12.34%	35
$LiInP_2O_7$:0.04Cr^{3+}	860	165	19.5	48	22%@383	6.24 mW@2.20%	36
$LiScP_2O_7$:0.06Cr^{3+}	880	170	∼38	∼37	∼23%@383	19 mW/7%	37
$NaInP_2O_7$:0.04Cr^{3+}	870	150	28.2	49.82	42.3%@373	9.08 mW/∼4.85%	38
Ca_2InTaO_6:0.02Cr^{3+}	880	200	33.6	30.6	34%@373	—	39
$CaScAlSiO_6$:0.01Cr^{3+}	950	205	30	31	77%@373	—	10

generally two potential mechanisms that can explain the enhanced absorption efficiency in Cr^{3+}-doped phosphors. One mechanism involves increasing the Cr^{3+} concentration to higher levels, which enhances absorption without inducing quenching effects. The other mechanism is the introduction of parity states through lattice distortion, breaking the forbidden transitions, which may be related to lattice distortion caused by [Cr^{3+}–Cr^{3+}] replacing [Mg^{2+}–Sn^{4+}].

To assess the application potential of LMSO:Cr^{3+} phosphors, we combined the optimized LMSO:0.06Cr^{3+} phosphor with a 450 nm blue InGaN chip to fabricate a pc-NIR LED device (as shown in the inset of Fig. 5a). The fabricated LED device was driven by currents ranging from 10 to 150 mA, as illustrated in Fig. 5a. As the current increased, both the near-infrared emission intensity and the corresponding near-infrared output power gradually increased before eventually reaching saturation. When the driving current is increased, the intensity of blue light emitted by the LED chip also rises, necessitating the phosphor to absorb more blue light and convert it to other wavelengths. However, the conversion efficiency of the phosphor is limited, and as the number of absorbed photons increases, the phosphor enters a saturation state, thereby constraining the final output power. Moreover, the temperature of the pc-LED device significantly rises under high current conditions. The increase in temperature leads to a decline in the quantum efficiency of the phosphor, with part of the energy being dissipated as heat rather than being converted into visible light. Additionally, the luminous efficiency of the LED chip itself decreases as the junction temperature rises, further exacerbating the saturation effect on output power. In the pc-LED, some photons emitted by the phosphor may also be reabsorbed, further limiting the increase in output power. However, due to the efficiency decay effect of the LED chip, the photoelectric conversion efficiency decreases as the current increases (Fig. 5b). Ultimately, the fabricated near-infrared pc-LED device achieves a near-infrared power of 25.20 mW at a driving current of 100 mA, with an optical conversion efficiency of 14.71% at a driving current of 10 mA. Due to the high

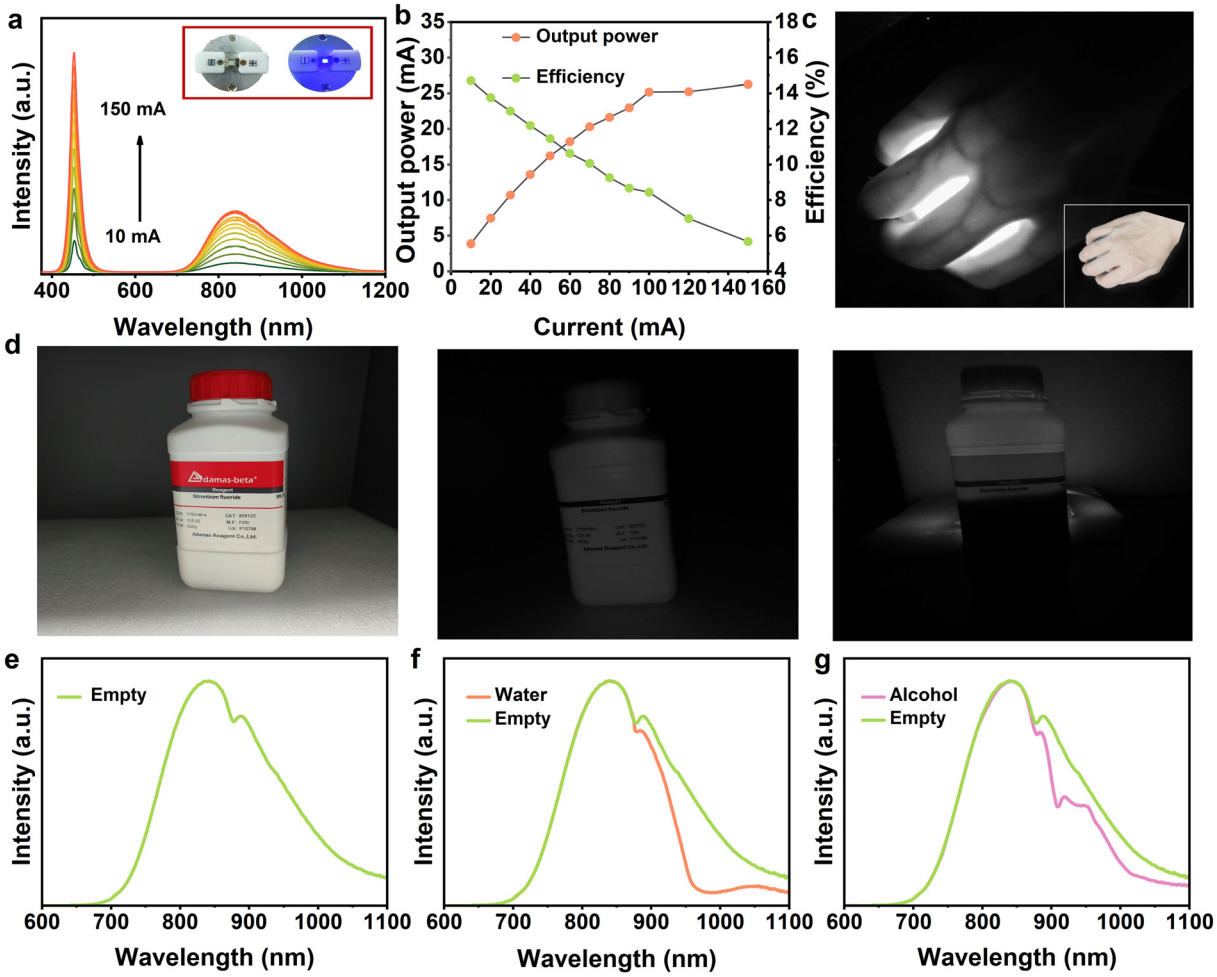

Fig. 5 (a) Electroluminescence spectra of the fabricated NIR pc-LED at various drive currents. The insets show photographs of the NIR light sources with power off and on; (b) output power and photoelectric conversion efficiency under various drive currents; (c) photographs of a human palm after being penetrated by the light of the LMSO:0.06Cr^{3+} phosphor from NIR pc-LED; (d) visible and near-infrared images of opaque plastic bottles illuminated by fluorescent lamps and manufactured near-infrared pc-LED lamps; (e–g) transmission spectra of NIR light after penetrating water and alcohol, respectively.

penetration and unique spectral properties of NIR light in biological tissues, we have further explored the potential applications of assembled NIR LED light in near-infrared spectroscopic detection and night vision. As shown in Fig. 5c, the NIR light emitted from the LED device can penetrate the palm of a human hand, enabling the identification of blood vessel distribution using an NIR camera. Additionally, we can accurately assess the degree of filling of opaque objects under the NIR light source, as demonstrated in Fig. 5d. Moreover, we fabricated a NIR pc-LED as a light source with a spectral range that effectively covers the characteristic absorption of multiple molecular vibrations. For compositional analysis, we selected two specific compounds, water and ethanol. The peak at 875 nm in Fig. 5e corresponds to the absorption of the sample tank. Fig. 5f shows an absorption peak at about 960 nm, representing the second harmonic absorption band of the O–H group. Besides the second harmonic absorption band of the O–H group at 950–1100 nm in the alcohol sample, an absorption band corresponding to the third harmonic of the C–H group at 900 nm is evident in Fig. 5g, further confirming the presence of ethanol. Furthermore, we have observed that light sources with different peak wavelengths exhibit varying sensitivities in detecting absorption signals. Thus, LMSO:Cr^{3+} phosphors are potentially valuable in the detection of target analytes with specific absorption signals.

4 Conclusions

In summary, we have prepared a series of doped LMSO:Cr^{3+} NIR phosphors by a solid-state reaction method and achieved broadband emission. The optimal sample LMSO:0.06Cr^{3+} has an emission band at about 860 nm under blue light excitation, a FWHM of 187 nm, and internal and external quantum efficiencies of 53.77% and 31.72% under 435 nm excitation, respectively. The excitation spectrum of LMSO:Cr^{3+} shows broadband absorption energy in the 400–500 nm region that matches that of the blue chip. The pc-LED device integrating the LMSO:Cr^{3+} phosphor and the 450 nm blue chip achieves a photoelectric efficiency of 14.71%@10 mA and an NIR output power of 25.20 mW@100 mA.

Data availability

Crystallographic data for $Li_{1.6}Mg_{1.6}Sn_{2.8}O_8$ has been deposited at the ICSD under ICSD.100590.

Conflicts of interest

The authors declare no conflict of interest.

Acknowledgements

This work is financially supported by the National Key Research and Development Program (Grant No. 2022YFC2905201), the National Natural Science Foundation of China (Grant No. 52072363 and 22305250), and the Key Laboratory of Rare Earths, Chinese Academy of Sciences.

Notes and references

1 G. Liu, M. S. Molokeev, B. Lei and Z. Xia, *J. Mater. Chem. C*, 2020, **8**, 9322–9328.
2 T. Wang, Y. Wang, W. Chen and Z. Xia, *Laser Photonics Rev.*, 2024, **18**, 2300784.
3 W. J. Gan, L. Y. Cao, S. M. Gu, H. W. Lian, Z. G. Xia and J. Wang, *Chem. Mater.*, 2023, **35**, 5291–5299.
4 Y. Zhang, S. H. Miao, Y. J. Liang, C. Liang, D. X. Chen, X. H. Shan, K. N. Sun and X. J. Wang, *Light: Sci. Appl.*, 2022, **11**, 136.
5 J. Qin, J. Xiang, H. Suo, Y. Chen, Z. Zhang, X. Zhao, Y. Wu and C. Guo, *J. Mater. Chem. C*, 2019, **7**, 11903–11910.
6 A. Kalinichev, M. Kurochkin, E. Golyeva, A. Kurochkin, E. Lähderanta, M. Mikhailov and I. Kolesnikov, *J. Lumin.*, 2018, **195**, 61–66.
7 R. Rao, *J. Lumin.*, 2005, **113**, 271–278.
8 Y. Yang, Z. Z. Lu, H. Fan, M. H. Chen, L. Shen, X. G. Zhang, Q. Pang, J. H. Chen, P. C. Chen and L. Y. Zhou, *Inorg. Chem.*, 2023, **62**, 3601–3608.
9 F. Y. Zhao, Z. Song and Q. L. Liu, *Int. J. Miner., Metall. Mater.*, 2022, **29**, 1286–1294.
10 G. Liu, M. S. Molokeev and Z. Xia, *Chem. Mater.*, 2022, **34**, 1376–1384.
11 S. Liu, J. Du, Z. Song, C. Ma and Q. Liu, *Light: Sci. Appl.*, 2023, **12**, 181.
12 Z. Wu, J. Xiang, C. Chen, Z. Li, X. Zhou, Y. Jin and C. Guo, *Ceram. Int.*, 2024, **50**, 5242–5249.
13 H. T. Zeng, T. L. Zhou, L. Wang and R. J. Xie, *Chem. Mater.*, 2019, **31**, 5245–5253.
14 S. Wang, R. Pang, X. Chen, T. Tan, Q. Wang, C. Li, S. Zhang, T. Tan, H. You and H. Zhang, *Ceram. Int.*, 2024, **50**, 1452–1460.
15 L. A. W. Shen, Y. Yang, M. H. Chen, Z. Z. Lu, H. Fan, X. G. Zhang, Q. Pang, F. W. Mo, L. Y. Zhou and P. C. Chen, *J. Alloys Compd.*, 2023, **969**, 172381.
16 Y. Wang, Y. Sun, Z. Xu, X. Xing and M. Shang, *Inorg. Chem.*, 2024, **63**, 8899–8907.
17 J. Y. Zhong, C. J. Li, W. R. Zhao, S. H. You and J. Brgoch, *Chem. Mater.*, 2022, **34**, 337–344.
18 Q. Q. Zhang, D. J. Liu, P. P. Dang, H. Z. Lian, G. G. Li and J. Lin, *Laser Photonics Rev.*, 2022, **16**, 2100459.
19 T. Tan, S. Wang, J. Su, W. Yuan, H. Wu, R. Pang, J. Wang, C. Li and H. Zhang, *ACS Sustainable Chem. Eng.*, 2022, **10**, 3839–3850.
20 L. You, R. D. Tian, T. L. Zhou and R. J. Xie, *Chem. Eng. J.*, 2021, **417**, 129224.
21 D. L. Dexter, *J. Chem. Phys.*, 1953, **21**, 836–850.
22 Z. H. Yue, D. S. Sun, Z. Lyu, S. D. Shen, C. Lyu, P. C. Luo and H. P. You, *J. Mater. Chem. C*, 2023, **11**, 16563–16570.
23 C. S. Zhong, L. Zhang, Y. H. Xu, X. D. Wu, S. W. Yin, X. B. Zhang and H. P. You, *J. Alloys Compd.*, 2022, **903**, 163945.

24 X. Wang, Y. Zhao, M. Yin, T. Zhou and R.-J. Xie, *J. Phys. Chem. C*, 2023, **127**, 22799–22807.
25 L. Q. Yao, Q. Y. Shao, M. L. Shi, T. Q. Shang, Y. Dong, C. Liang, J. H. He and J. Q. Jiang, *Adv. Opt. Mater.*, 2022, **10**, 2102229.
26 H. Cai, S. Liu, Z. Song and Q. Liu, *J. Mater. Chem. C*, 2021, **9**, 5469–5477.
27 T. Liu, H. Cai, N. Mao, Z. Song and Q. Liu, *J. Am. Ceram. Soc.*, 2021, **104**, 4577–4584.
28 H. Y. Wu, L. H. Jiang, K. Li, C. Y. Li and H. J. Zhang, *J. Mater. Chem. C*, 2021, **9**, 11761–11771.
29 I. Baginskiy and R. S. Liu, *J. Electrochem. Soc.*, 2009, **156**, G29–G32.
30 S. Wei, Z. Y. Lyu, D. S. Sun, S. D. Shen, X. W. Zhang, Z. Lu, P. C. Luo, H. Y. Hu and H. P. You, *J. Mater. Chem. C*, 2024, **12**, 4977–4985.
31 X. X. Xu, Q. Y. Shao, L. Q. Yao, Y. Dong and J. Q. Jiang, *Chem. Eng. J.*, 2020, **383**, 123108.
32 C. J. Li and J. Y. Zhong, *Chem. Mater.*, 2022, **34**, 8418–8426.
33 G. Chen, W. Nie, J. Zuo, Y. Li, L. Han and X. Ye, *Dalton Trans.*, 2022, **51**, 12576–12584.
34 J. A. Lai, W. H. Shen, J. B. Qiu, D. C. Zhou, Z. W. Long, Y. Yang, K. Zhang, I. Khan and Q. Wang, *J. Am. Ceram. Soc.*, 2020, **103**, 5067–5075.
35 F. Zhao, H. Cai, Z. Song and Q. Liu, *Chem. Mater.*, 2021, **33**, 3621–3630.
36 H. Zhang, J. Zhong, X. Zhang, H. Yang, Z. Mu and W. Zhao, *J. Alloys Compd.*, 2022, **894**, 162386.
37 L. Yao, Q. Shao, S. Han, C. Liang, J. He and J. Jiang, *Chem. Mater.*, 2020, **32**, 2430–2439.
38 L. Zeng, J. Zhong, C. Li, Z. Zhuang, L. Chen and W. Zhao, *J. Lumin.*, 2022, **247**, 118909.
39 J. Zhang, W. Zhao, X. Zhang, Y. Li, W. Zhang, H. Wen and J. Zhong, *J. Lumin.*, 2023, **255**, 119581.